# Laser-based long-wave-infrared hyperspectral imaging system for the standoff detection of trace surface chemicals

Anish K. Goyal
Derek Wood
Vincent Lee
Joshua Rollag
Peter Schwarz
Leyun Zhu
Gary Santora

# Laser-based long-wave-infrared hyperspectral imaging system for the standoff detection of trace surface chemicals

**Anish K. Goyal,*** **Derek Wood, Vincent Lee, Joshua Rollag,**
**Peter Schwarz, Leyun Zhu, and Gary Santora**
Block MEMS LLC, Southborough, Massachusetts, United States

**Abstract.** A trace chemical detector is described that combines external-cavity quantum cascade lasers and a mercury cadmium telluride camera to capture hyperspectral images of the diffuse reflectance from a target surface in the long-wave infrared. The system is able to generate individual hypercubes in <0.1 s. When raster scanning the laser beam over the target surface, areal coverage rates of >60 $cm^2$/s have been achieved. Results are presented for standoff distances ranging from 0.1 to 25 m. Hyperspectral images generated by the system are analyzed for spectral features that indicate the presence of trace surface contaminants. This approach has been found to be highly capable of detecting trace chemical residues on a wide variety of surfaces, and we present a collection of detection results to demonstrate the capabilities of this technology. Examples include the detection of 10 $\mu$g of saccharin powder on a wide range of substrates, 0.2 $\mu$g of an explosive residue on a computer keyboard, residual pharmaceuticals within a plastic baggie, and a contaminated fingerprint on cell phone case. © *The Authors. Published by SPIE under a Creative Commons Attribution 4.0 Unported License. Distribution or reproduction of this work in whole or in part requires full attribution of the original publication, including its DOI.* [DOI: 10.1117/1.OE.59.9 .092003]

## 1 Introduction

Standoff detection of trace chemicals on surfaces is of great importance for a variety of commercial, law enforcement, intelligence, and military applications, such as explosives detection, drug detection, forensic analysis, contamination avoidance, border protection, cleaning validation, and process monitoring.[1,2] Sensitive techniques, such as mass spectrometry and ion-mobility spectrometry, exist for trace chemical sensing, but these require a physical transfer of the chemicals into the instrument.[3,4] However, there are many situations in which physical sampling is not feasible and it is highly desirable to perform noncontact and nondestructive testing at appreciable standoff distances (>1 m).[5]

Of the demonstrated standoff detection methods, the most promising ones include laser-induced breakdown spectroscopy (LIBS),[6,7] Raman spectroscopy,[8–10] and long-wave infrared (LWIR) spectroscopy.[11,12] The LWIR approaches can be divided into those that are passive (utilizing ambient radiation)[13–15] and those that are active (utilizing illumination). The active illumination techniques can be further classified according to whether they measure the optical reflectance[16–29] or the photothermal effect.[30–33] The approach described in this paper is classified as actively illuminated LWIR reflectance spectroscopy.

Please refer to Ref. 2 and the references therein for a discussion of the trade-offs between these different approaches. Here, these trade-offs are discussed only briefly. LIBS measures the atomic constituents of a material by forming a plasma at the surface by illuminating it with an intense laser pulse. The plasma contains the surface chemicals that emit light at wavelengths that are characteristic of particular atoms. On the other hand, Raman and LWIR spectroscopies

---

*Address all correspondence to Anish K. Goyal, E-mail: anish.goyal@blockeng.com
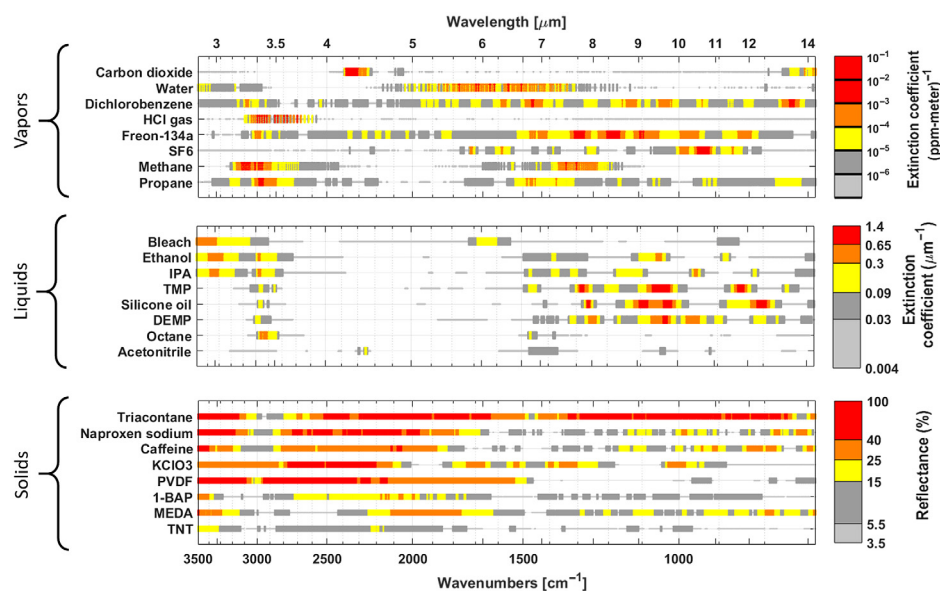
**Fig. 1** Color-coded plot of the MIR spectra for a selection of chemicals in vapor, liquid, and solid forms.

probe the vibrational modes of molecules. The molecular vibration spectrum is unique for each molecule, thus allowing chemicals to be identified. LWIR has the advantage of having very large optical cross-sections that are several orders of magnitude larger than those for Raman. This means that relatively low power LWIR lasers can be used to achieve high-sensitivity detection. For a more detailed comparison of Raman and LWIR spectroscopies for standoff detection, refer to Ref. 16. In brief, it is our opinion that LWIR reflectance spectroscopy is uniquely suited to combining high sensitivity chemical detection with the ability to rapidly scan surfaces with a high areal coverage rate (ACR) while remaining eye safe.

To illustrate the richness of LWIR spectra, Fig. 1 shows the spectra for a variety of vapors, liquids, and solids over the mid-infrared (MIR) band. The MIR band roughly corresponds to $\lambda \approx 2.8$ to 14 $\mu$m (about 3500 to 700 $cm^{-1}$). The MIR includes both the mid-wave infrared and LWIR atmospheric transmission windows, which approximately correspond to wavelength ranges of $\lambda \approx 3$ to 5 $\mu$m and 7 to 14 $\mu$m, respectively. The band between $\lambda \approx 5$ to 7 $\mu$m is not suitable for standoff detection because of strong absorption from atmospheric water vapor. A color-coded scheme is used in Fig. 1 to plot the absorption coefficient for vapors and liquids and the powder reflectance for solids. Note that, for solids, a lower reflectance is associated with a higher absorption coefficient. It can be seen that a majority of chemicals are well detected in the LWIR. The LWIR is the probably the most important band for standoff detection because of (i) the high degree of atmospheric transparency, and (ii) the existence of rich spectra for the largest fraction of chemicals of interest.

## 2 Method

### 2.1 Measurement Approach

As shown in Fig. 2, the detection approach described here involves actively illuminating the surface using a wavelength tunable, external-cavity quantum cascade laser (EC-QCL) and measuring the diffuse reflectance using a mercury cadmium telluride (MCT) camera. Since it is usually most favorable to measure the diffusely reflected light, the surface should be oriented such that the specularly reflected component is not returned to the camera. As the laser is tuned in wavelength, images are captured by the camera at each illumination wavelength to generate a hyperspectral image cube (i.e., hypercube). This raw measured hypercube is converted into a reflectance hypercube by appropriate normalization as described below. Each pixel of the reflectance hypercube contains the reflection spectrum for a point on the surface. Detection
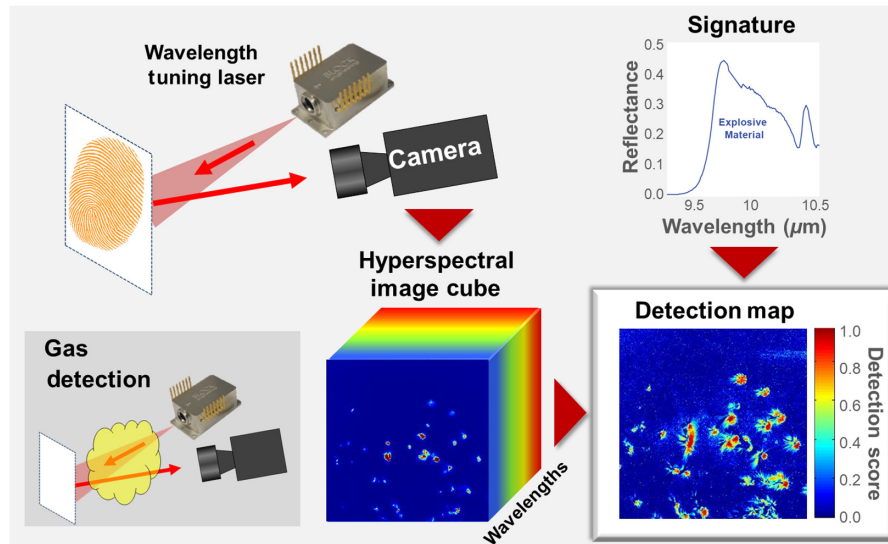
**Fig. 2** Measurement configuration for laser-based LWIR hyperspectral imaging.

algorithms are then applied to compare the measured spectra for each pixel in the hypercube with those in a spectral library. The result is a detection map that identifies and maps any chemical(s). Figure 2 shows an actual detection result for trace particles of $KClO_3$ on a metallic mirror at close range. As shown in Fig. 2, this approach can also be used to detect gases that are present between the sensor and the surface being illuminated.

The use of lasers to actively illuminate the target surface enables standoff detection at distances of at least tens of meters, while the use of a camera as the receiver enables mapping of the chemicals with high spatial resolution. The ability to map the chemical contamination with high spatial resolution significantly improves the detection performance when the chemical contamination is localized. In real-world scenarios, it is expected that localized contamination will be the most frequently encountered situation.

As mentioned earlier, the measured hypercube must be normalized to account for the illumination intensity pattern and system throughput to generate a reflectance hypercube.[20] This is accomplished by measuring a standard reference surface, such as roughened aluminum (rough-Al), which approximates a Lambertian reflector having near-unity reflectance. Referring to Fig. 3, normalization occurs by acquiring raw hypercubes for both the reference and sample surfaces. The thermal background (when there is no laser illumination) is first subtracted from frames with laser illumination. This step is critical because the magnitude of the thermal radiation in the LWIR is significant, often exceeding the active signal from the laser. The reflectance hypercube is then obtained by dividing the sample hypercube by the reference hypercubes on a pixel-by-pixel basis for each wavelength. This automatically accounts for the wavelength
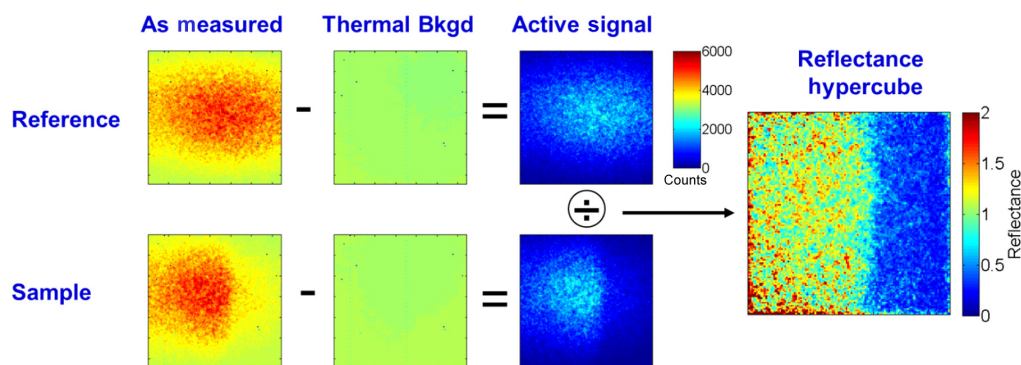


**Fig. 3** Method of converting a measured hypercube into a reflectance hypercube.

dependence of the laser power, beam shape, and optical throughput. One drawback of this method is that the speckle noise in the reference hypercube is transferred to the reflectance hypercube. To reduce this additional speckle noise, the reference hypercube is often smoothed prior to performing the division. The reflectance hypercube can then be said to be calibrated with respect to a diffuse reflectance standard.

## 2.2 Interaction with the Government Test and Evaluation Team

The work presented in this paper was supported by the Intelligence Advanced Research Projects Activity (IARPA) program called Standoff ILluminator for Measuring Absorbance and Reflectance Infrared Light Signatures (SILMARILS). Under this program, many of the component technologies were developed including lasers, electronics, software, and detection algorithms. In addition, the program incorporated a robust test and evaluation (T&E) component involving multiple organizations including the Naval Research Laboratory (NRL), Johns Hopkins University Applied Physics Laboratory (JHU/APL), and the Pacific Northwest National Laboratory (PNNL). These organizations were responsible for various activities including (i) generating samples using a variety of deposition methods with calibrated loadings of surface contaminants, (ii) measuring the optical constants of a wide range of chemicals, and (iii) developing signature models to predict the reflection spectra of particles on surfaces. All of these activities were essential for advancing the LWIR trace detection technology. Most of the samples described in this paper were prepared by NRL and JHU/APL. The PNNL reference spectra were used to determine the absorption line positions for each chemical.

## 2.3 System Configuration

The major components of the LWIR system shown in Fig. 2 include the laser, laser transmitter, camera, camera lens, control electronics, software, and detection algorithms. Each of these components has evolved over time during the course of the work presented in this paper. Therefore, in the following we simply provide a general description of the system.

The lasers are based on Block Engineering's commercially available Mini-QCL™, which is a miniature, widely tunable, high-speed, and rugged EC-QCL. Since the measurement speed (i.e., ACR) depends on laser power, under the SILMARILS program, we developed a new laser package that is capable of generating significantly more average power (i.e., >100 mW) than the commercially available laser package. Figure 4 shows a photograph of one of the newly developed high-power Mini-QCLs. Also shown is the composite tuning curve for three such lasers, which provide a total tuning range of 923 to 1400 cm$^{-1}$ ($\lambda = 7.1$ to 10.8 $\mu$m). These lasers operate under pulse conditions with maximum peak powers of about 1 W under conditions of low duty factor (100-ns pulse length and 1% duty factor). The maximum average power at the peak of the gain curve exceeds 100 mW. Some of the recent results presented in this paper utilize these new high-power lasers. Most of the results, however, were made by combining the output from a pair of commercially available Mini-QCLs to span $\lambda = 7.7$ to 11.8 $\mu$m. When multiple EC-QCLs are used, their beams are spatially overlapped using combination optics.
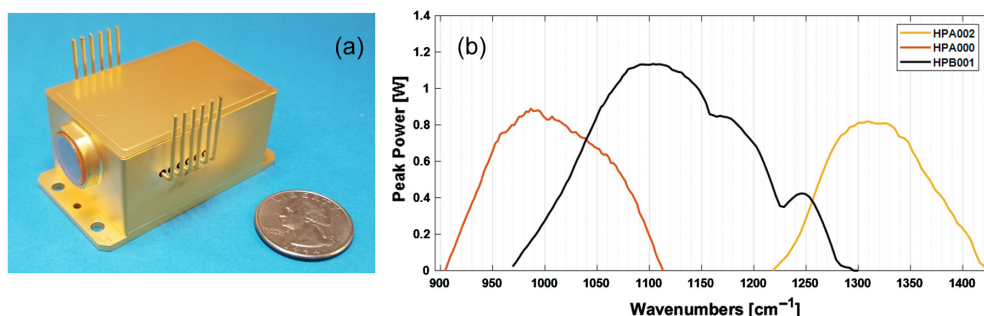


**Fig. 4** (a) Photograph of a miniature high-power EC-QCL and (b) tuning curves of three EC-QCLs, which provide a total tuning range of 925 to 1400 cm$^{-1}$ (7.1 to 10.8 $\mu$m).

The beam from the laser source is directed to a transmitter that comprises a telescope and an X-Y galvo-scanner to raster-scan the laser beam over the target surface. The transmitter also has a variable focus to allow adjustment of the beam size at the surface.

Light that is diffusely reflected from the surface is captured by a $LN_2$-cooled MCT focal-plane array having $128 \times 128$ pixels with a pitch of 40 $\mu$m. It is capable of capturing full frames at rates of up to 1.6 kHz. In windowed mode, windows of $16 \times 96$ pixels can be captured at 9.4 kHz. The camera is typically fitted with a 200-mm focal length lens for standoff distances of >5 m. The spatial resolution of the image is referred to as the ground sampling distance (GSD). At a standoff distance of 5 m, the GSD = 1 mm. The GSD increases approximately linearly with increasing distance. For shorter standoff distances, several different optical arrangements have been used. The smallest standoff distance used was typically 0.1 m with a corresponding GSD = 80 $\mu$m.

A custom electronics controller is responsible for coordinating laser firing and wavelength control with triggering of the camera. For each frame of the hypercube, the lasers are typically driven in burst mode during the integration period of each camera frame.

It is a goal of the SILMARILS program to achieve chemical imaging at video frame rates. That is, a detection map is generated 30 times per second for a sample at a 5-m standoff. There is also a goal of measuring a 1-m$^2$ area at a 30-m standoff within 15 s. While these goals have not yet been demonstrated, we believe that these goals can be achieved using the currently existing hardware.

## 2.4 Description of Hypercube Acquisition

In this section, the process of acquiring hypercubes is described through the use of videos. First, an example of the acquisition of a single hypercube is given. Then, to scan larger areas, the laser beam is raster scanned across the surface, and hypercubes are captured at each scan position. These individual hypercubes are combined to form a larger composite hypercube. Finally, an example is shown of capturing a composite hypercube at very high speeds.

Figure 5 gives an example reflectance hypercube of a rough-Al sample in which the right-half of the sample is lightly coated with silicone grease.[21] Measurements are made at a standoff distance of 0.1 m with a measurement area of 1 cm$^2$ and GSD = 80 $\mu$m. A single laser illuminates the sample from 7.4 to 10.5 $\mu$m, and hypercube frames are captured in steps of 0.02 $\mu$m. The camera was operated at a frame-rate of 1.6 kHz. The measurement hypercube consisted of 137 frames with laser illumination plus 13 "dark" frames for measurement of the thermal background. Video 1 is a time-lapse video that shows how the reflectance evolves as a function


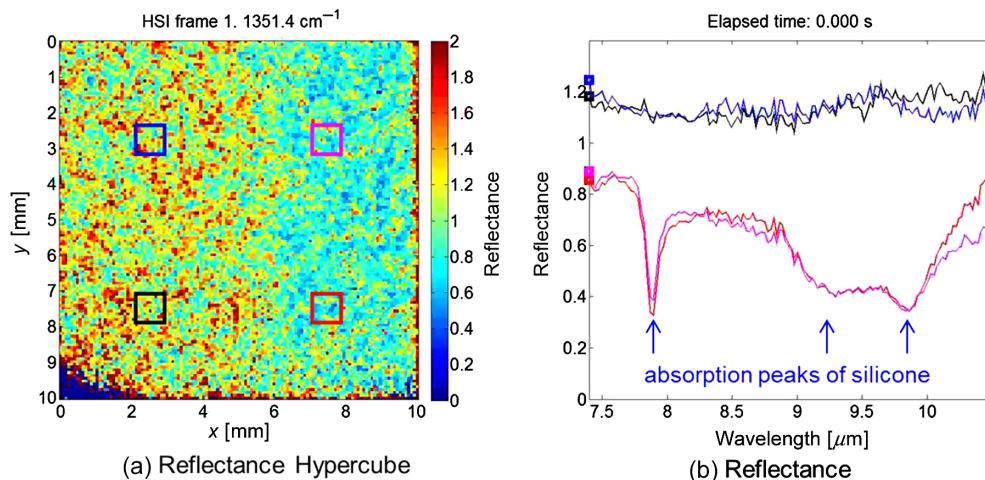
(a) Reflectance Hypercube

(b) Reflectance

**Fig. 5** Example of a hypercube acquisition for silicon grease on rough aluminum. (a) The reflectance hypercube and (b) the reflection spectrum from four different locations. Video 1 shows a video of the hypercube (Video 1, 13.8 MB, MP4 [URL: https://doi.org/10.1117/1.OE.59.9.092003.1]).
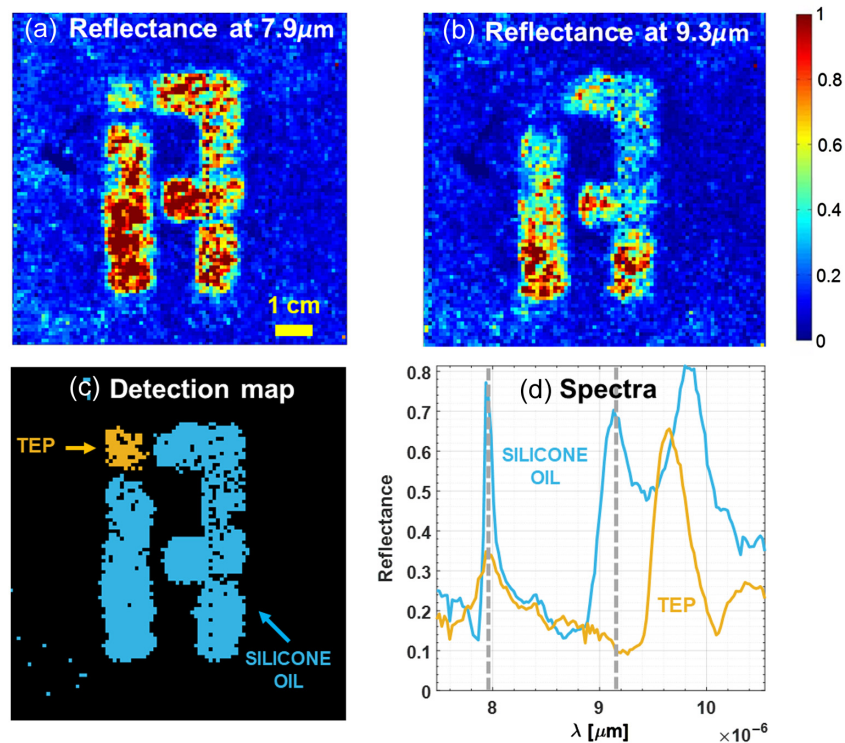
**Fig. 6** Composite hypercube that depicts the IARPA logo drawn onto HDPE using two different chemicals: (a) reflectance image at 7.9 $\mu$m, (b) reflectance image at 9.3 $\mu$m, (c) detection map indicating the two different chemicals, and (d) reflection spectra for the two different chemicals. Video 2 shows sample preparation, acquisition, and the resulting hypercube (Video 2, 13.3 MB, MP4 [URL: https://doi.org/10.1117/1.OE.59.9.092003.2]).

of wavelength. The total acquisition time was only 0.095 s. The absorption lines of silicone are clearly seen in the spectra for the contaminated area while the spectra in the clean area are essentially featureless.

Figure 6 shows the acquisition of a composite hypercube.[21] To measure large areas, it is necessary to raster scan the laser beam across the sample. For this example, the sample consists of a 10-cm-square piece of high-density polyethylene (HDPE) onto which the logo for our IARPA sponsor was drawn using two different chemicals: silicone oil and triethyl phosphate. In this example, the camera as fitted with an $f = 200$ mm lens and measurements were made at a standoff distance of 5.3 m with GSD = 1 mm. The laser beam was raster scanned over a $7 \times 7$ array of positions to cover an area of 80 cm$^2$. At each measurement location, a hypercube with 137 wavelengths was acquired as described in the previous example. The total acquisition time for the $7 \times 7$ array was <8 s. The individual hypercubes were then combined to form a composite hypercube. Figure 6 shows individual frames of the reflectance hypercube at wavelengths 7.9 and 9.3 $\mu$m. Figure 6(d) shows that the spectra for these two chemicals are easily differentiated, allowing for the generation of the detection map shown in Fig. 6(c). The vertical dashed lines in Fig. 6(d) correspond to the two frames of the hypercube that are shown. In one image, the "dot" in the IARPA logo is visible while in the other image it is not. The video associated with this figure shows the process sample fabrication, the measurement, and the resulting hypercube. The green laser, which is seen during the measurement, is simply a pointer laser that overlaps the LWIR beam (which is not visible).

Finally, Fig. 7 shows an example of very high-speed acquisition of a composite hypercube at 5.3-m standoff. In this case, the camera was operated in windowed mode to acquire $32 \times 128$ pixels at a frame rate of 6.2 kHz. The camera window was moved during acquisition to track the location of the laser illumination to generate a composite hypercube of the entire sample ($96 \times 96$ pixels). At each position, the acquisition time was only 15 ms for a hypercube with 79 wavelengths, and the time needed to point to subsequent spots was 5 m. This corresponds to a
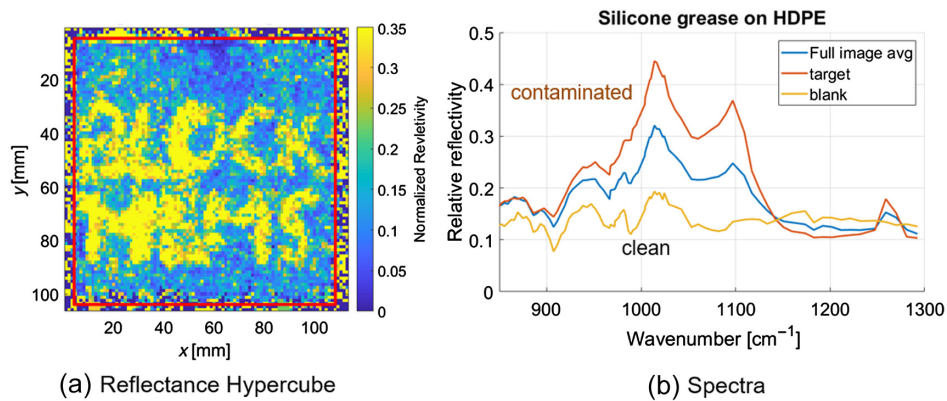
(a) Reflectance Hypercube

(b) Spectra

**Fig. 7** Very high-speed acquisition of a composite hypercube of an HDPE sample with words written in silicone grease: (a) reflectance of the sample at 11.6 $\mu$m and (b) spectra averaged over different regions. Video 3 shows the acquisition process at the actual measurement speed (Video 3, 0.9 MB, MP4 [URL: https://doi.org/10.1117/1.OE.59.9.092003.3]).

hypercube measurement rate of 50 Hz. Since the beam was scanned over $9 \times 9$ positions to measure an area of 100 cm$^2$, the total measurement time was 1.62 s, and the corresponding measurement speed was ACR $= 62$ cm$^2$/s. Video 3 associated with this figure shows the actual acquisition process. As before, the red laser beam is only to aid in visualization since the LWIR beam is not visible. The sample that was measured consisted of a 10-cm-square piece of HDPE onto which the letters "BLOCK MEMS" were written using silicone grease. Video 3 shows a frame of the hypercube at a wavelength of 11.6 $\mu$m as well as spectra associated with different regions. The yellow curve corresponds to the reflectance of clean HDPE. The orange curve corresponds to the regions of silicone contamination; the two strong upward going peaks are due to silicone. The intermediate curve corresponds to the average reflectance over the entire sample. To the best of our knowledge, this represents the highest ACR ever demonstrated for this active LWIR hyperspectral technology. Using the currently existing high-power lasers, the laser beam size can be increased to achieve even higher ACR.

## 3 Measurement Examples

In this section, various measurement results are presented. First, there is a discussion of LWIR reflectance signatures. Then, examples are given of measuring uniformly contaminated samples. And finally, examples are given of mapping chemical contamination that is localized.

### 3.1 Complexity of Reflectance Signatures

The LWIR reflection spectrum from a contaminated surface depends on many factors including the substrate material and its roughness, the chemical(s) and their presentation, and measurement geometry.[34–39] In this section, these factors are briefly discussed.

Figure 8 shows the reflection spectra for various substrates as measured using the setup described in this paper. Each substrate has a unique reflection spectrum. It is easier to detect trace chemicals on substrates that have relatively featureless spectra. It becomes more difficult to detect chemicals when the substrate itself has a complex reflection spectrum of its own. Plastics and polymeric fabrics have been found to have highly variable spectra. A particularly challenging substrate is Delrin® (polyoxymethylene), which has a polarization-dependent reflectance. Figure 9 shows the measured reflection spectra for Delrin in two orthogonal laser beam polarizations (disregard the line color). This significantly complicates the ability to detect and identify trace chemicals on Delrin.

Another factor that affects detection performance is the roughness of the substrate surface. A smooth surface will have little or no measurable diffuse reflectance. This is particularly advantageous when measuring a sparse distribution of particles on the surface because the signal from
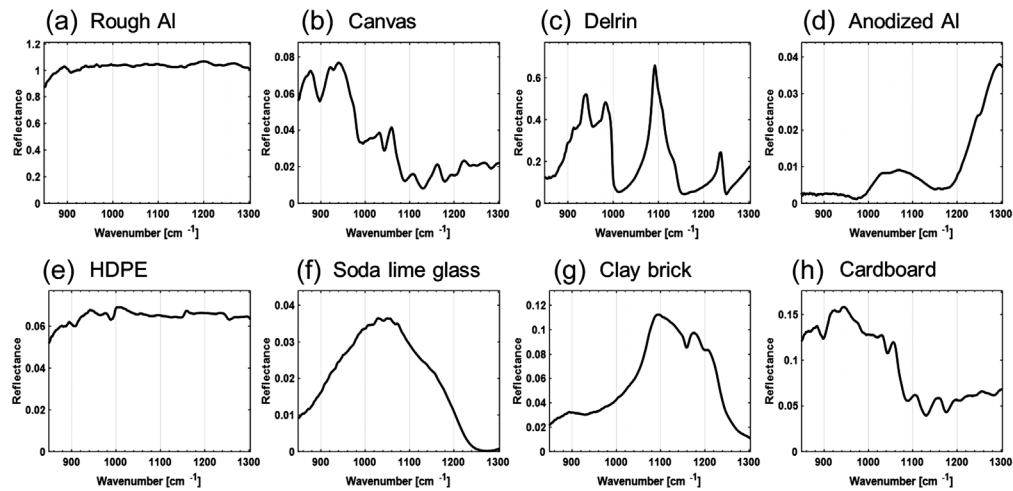
**Fig. 8** Reflection spectra for various substrates including (a) rough Al, (b) canvas, (c) delrin, (d) anodized Al, (e) HDPE, (f) soda lime glass, (g) clay brick, and (h) cardboard.
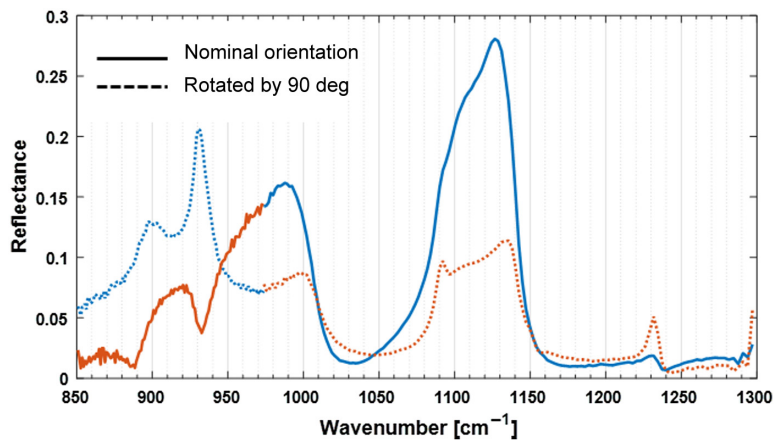


**Fig. 9** Reflection spectrum of Delrin in two orthogonal polarizations.

these particles (which carries the chemical signature to be detected) is not overwhelmed by the signal from the clean substrate. Furthermore, smooth surfaces will reduce speckle noise that would otherwise interfere with the identification of spectral features associated with trace chemicals.[16] It is usually easiest to detect trace chemicals on smooth surfaces except for the case where the contamination presents itself as highly uniform thin films having minimal diffuse scatter. Rough surfaces, by contrast, have the advantage of generating a large diffuse reflection signal, which means that the laser illumination intensity can be reduced. This allows one to use larger beam sizes and thereby increase the ACR.

The substrate can also have a significant impact on the shape of the reflection spectrum. Figure 10 shows the measured reflectance for a thin layer of silicone oil on both HDPE and rough-Al. The reflectance is plotted for various samples angles with 0 deg corresponding to the case in which the specularly reflected beam is collected by the camera. The vertical dashed lines correspond to the absorption peaks of silicone. For silicone on HDPE, the absorption peaks of silicone are associated with enhanced reflectance from this dielectric substrate. This phenomenon is counterintuitive since one expects that the reflected signal should decrease at the absorption lines. Nevertheless, this behavior is fully consistent with theoretical calculation of the response for a thin film on a dielectric substrate.[37] Since the HDPE samples are relatively smooth, the magnitude of the reflectance decreases with increasing sample angle. For silicone on rough-Al, the expected downward features at the absorption peaks of silicone are observed when the sample angle is sufficiently steep. For angles close to 0 deg, one observes an
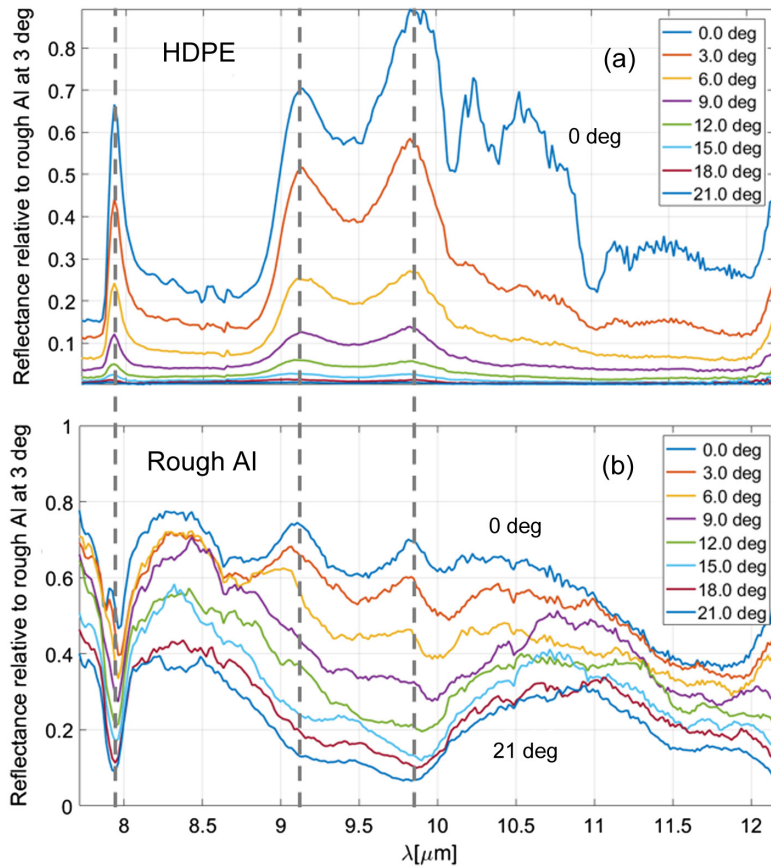
**Fig. 10** Reflection spectra for a thin layer of silicone oil on (a) HDPE and (b) rough-Al. Spectra are plotted for various values of the sample angle relative to angle corresponding to a specular reflection of 0 deg.

enhancement of the reflectance at the absorption peaks of silicone. This dataset demonstrates essential aspects of signature complexity for a thin film dielectric and metallic surfaces.

Figure 11 plots the reflection spectra for sieved particles of trimethylene-trinitramine (RDX) and pentaerythritol-tetranitrate (PETN) on glass. The reflection spectrum is essentially that of the underlying glass substrate (which has a peak reflectance at roughly 1050 $cm^{-1}$ due to the Reststrahlen effect) with the chemical signature manifesting itself as a reduced reflectivity at the chemical's absorption lines. This situation has been modeled using a modified Mie-scattering
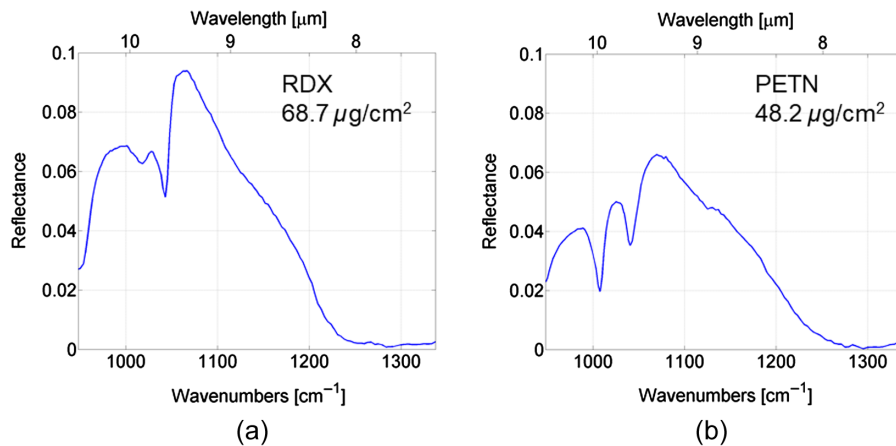


**Fig. 11** Reflection spectra for (a) RDX and (b) PETN, both deposited as sieved particles onto glass.
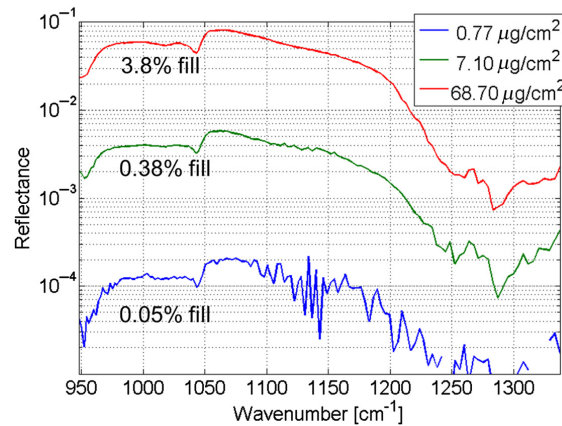
**Fig. 12** Reflection spectra for particles of RDX on glass for various mass loadings.

formalism,[36] and the measured spectra are found to be in reasonable agreement with the Mie-scattering calculation even though the actual particles are irregularly shaped and are not spherical. Since the clean glass substrate has a negligible diffuse reflectance component, the measured signal arises due to scattering from the particles themselves. Therefore, it is expected that the magnitude of the reflectance should be proportional to the areal density of particles. Figure 12 shows a semilogarithmic plot of the reflectance for RDX particles on glass for mass loading that varies from 0.8 to 69 $\mu$g/cm$^2$. As expected, the magnitude of the reflectance varies approximately linearly with loading while the spectral shape remains unchanged. Note that the fill factor of particles at the lowest loading is only 0.05%. Note also that, in this case, the hyperspectral imaging sensor is able to measure the reflectance with a noise floor below $10^{-4}$.

The morphology of the chemical contamination is referred to here as the chemical "presentation." Figure 13 shows photomicrographs of caffeine deposited onto glass using two different methods. Figure 13(a) shows the result of solvent deposition in which caffeine is dissolved in a solvent and then applied to the glass via air-brushing. The solvent evaporates leaving behind a film of caffeine. Under magnification, it is observed that the caffeine film consists of a dense arrangement of polycrystalline fibers. Different chemicals are found to form polycrystalline films having a wide range of morphologies. Figure 13(b) shows sieved particles of caffeine. Figure 13(c) compares the reflectance of these two samples. The overall shape of the reflectance is due to the Reststrahlen band of silica, and the difference in the shape for these two samples is probably due to the difference in the type of glass used, although this has not been confirmed. The main aspect to note is that the spectral features are of two kinds: absorptive or dispersive. The vertical lines in the plot correspond to the absorption lines of caffeine. For sieved particles, the local minima of the chemical's spectral features are centered on the absorption lines
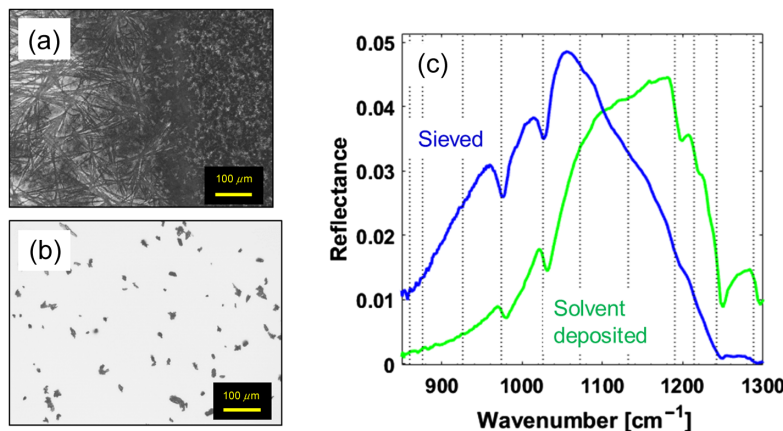


**Fig. 13** Photomicrographs of caffeine deposited onto glass using (a) solvent deposition and (b) sieving of particles at loadings of 76 and 24 $\mu$g/cm$^2$, respectively; (c) their reflection spectra.

as expected. For the solvent-deposited samples, the spectrum has a dispersive shape with a region of anomalous dispersion, which is centered on the absorption line. This results in the local minima being offset toward higher wavenumbers (shorter wavelengths). Such a dispersive feature would be expected for the first-surface reflectance from a thick film.[20] Upon close inspection of these spectra, one can see hints of most of the absorption lines associated with caffeine.

### 3.2 Additional Examples of Uniform Contamination

In this section, two examples are given in which the hypercube is analyzed by simply measuring the average reflectance from the sample. The first example demonstrates that high quality spectra can be obtained at standoff distances of tens of meters. The second example demonstrates that many commercially used plastic bags are highly transparent in the LWIR, and the contents can be identified using this technology.

Figure 14 shows the reflectance spectrum of solution-deposited saccharin on glass when measured at a standoff distance of 25 m. The chemical signature of saccharin can clearly be seen when compared with the imaginary part of its refractive index (which is proportional to the absorption coefficient). Based on the precise location of the spectral features, it is observed that the features have a dispersive shape. The primary impact of making this measurement at longer standoff distances is that there are fewer pixels that interrogate the target, which, in turn, increases the noise. For the measurement shown in Fig. 14, $\tilde{3}00$ pixels are averaged over a 75-mm-square region at the target. Despite the relatively few pixels, the spectrum is of high quality.

Figure 15 shows the detection of benzocaine within a plastic "mini-bag." These measurements were made at close range with GSD = 80 $\mu$m and with the laser beam incident onto the sample at an angle of about 30 deg. Figures 15(a) and 15(b) show photographs of when the benzocaine fills the minibag as a bulk powder and when it is "emptied" to have an average loading of only 20 $\mu$g/cm$^2$. The reflectance is plotted both scaled and offset (to aid in display) for several cases. The top 2 curves compare the reflectance of benzocaine as a bulk powder both with and without the minibag. The shapes of the two spectra are virtually identical, showing that the minibag is virtually transparent to the measurement system. We believe that interference fringes that could arise due to the minibag are not observed because of the relatively steep illumination angle. The spectrum of benzocaine is clearly observed even as the loading is progressively reduced to 20 $\mu$g/cm$^2$. Given that the GSD = 80 $\mu$m, this loading corresponds to detecting masses as low as 2 ng on a per-pixel basis.
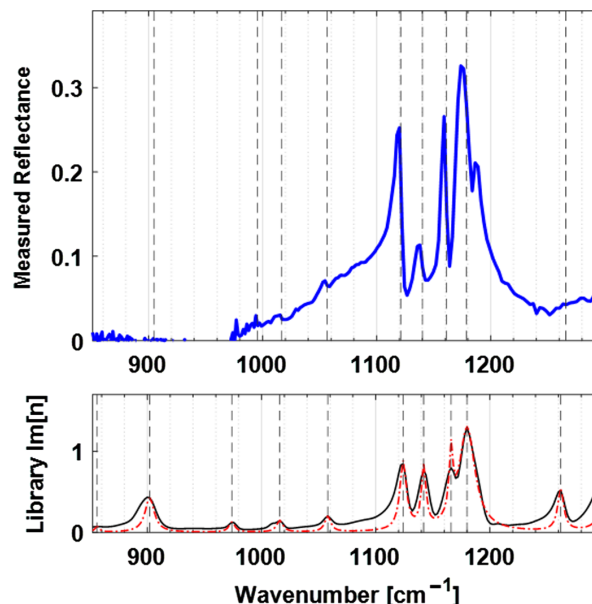


**Fig. 14** Reflectance of 98 $\mu$g/cm$^2$ of solution-deposited saccharin on glass at a standoff distance of 25 m.

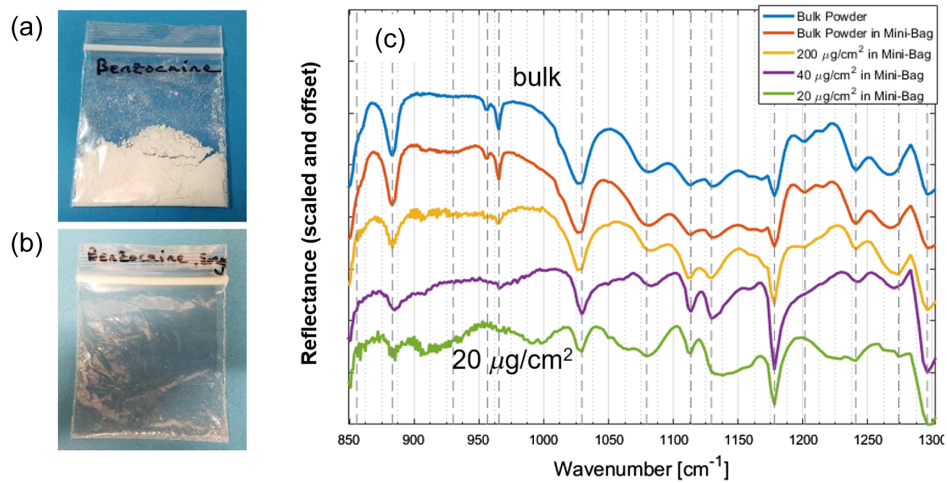**Fig. 15** Photographs of benzocaine powder in a minibag as (a) bulk powder, (b) with average areal concentration of 20 $\mu$g/cm$^2$, and (c) comparative spectra.

### 3.3 *Locally Contaminated Samples*

In this section, several examples are given to demonstrate mapping of localized contamination. First, the approach taken to analyze the hypercubes is summarized. Then, examples are given of (i) saccharin dry transferred onto a wide variety of substrates, (ii) a caffeine-contaminated finger-print on a cell phone case, (iii) the dry transfer of PETN onto keyboard keys, and finally (iv) the dry transfer of multiple chemicals onto concrete.

    Figure 16 summarizes the algorithmic approach used to map localized contamination. This example corresponds to sample of saccharin that was dry transferred onto packing tape. Figure 16(a) shows a single frame of the measured reflectance hypercube. The hypercube is
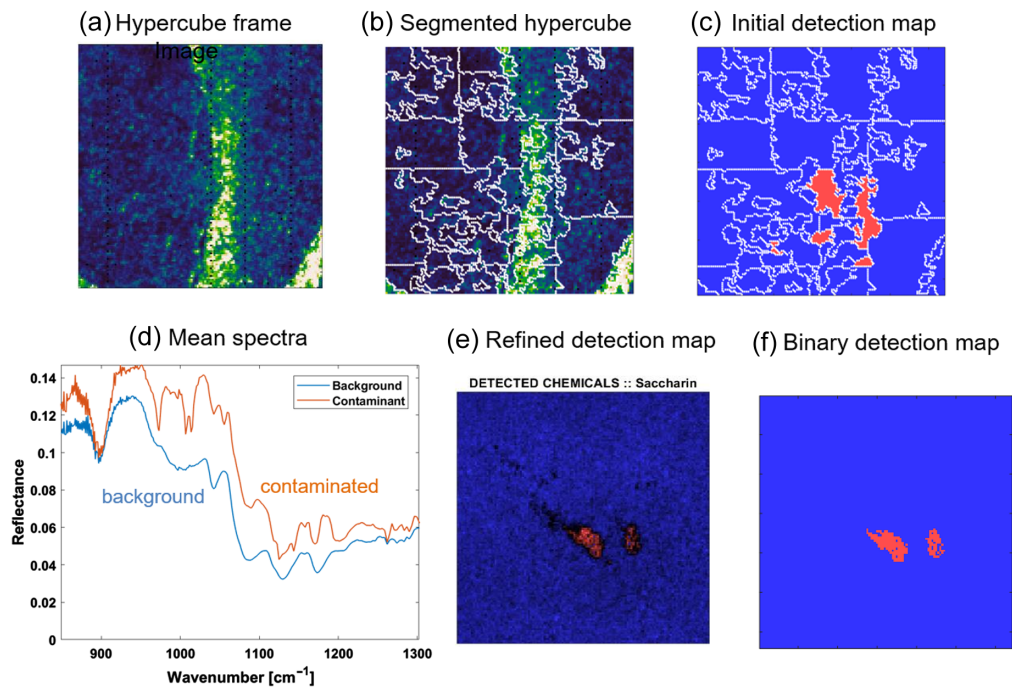


**Fig. 16** The algorithmic steps to mapping localized contamination are illustrated in this figure. The steps involve (a) capturing the hypercube, (b) segmenting the hypercube based on spectral similarity, (c) creating an initial detection map based on the (d) mean spectra in the various segments, (e) refining the detection map, and finally (f) creating a binary detection map. Note that each of these images represent an area of 1 cm$^2$.
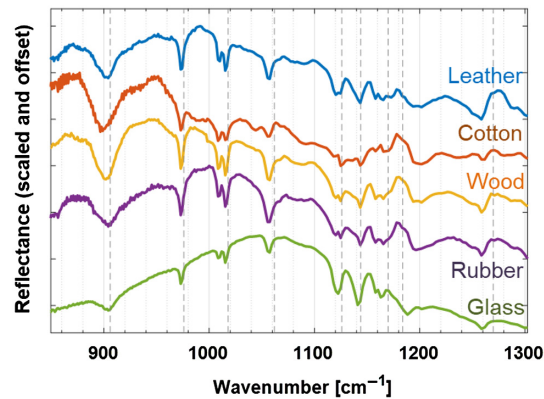
**Fig. 17** Reflection spectra (scaled and offset) for 10 $\mu$g of saccharin that is dry transferred on to various substrates demonstrates that the spectral features due to saccharin are consistently observed.

analyzed using an algorithm that divides the image into segments based on the spectral similarity in adjacent pixels. Analysis of the spectra in each of the segments then allows regions to be identified as either clean or contaminated. By comparing the two spectra in Fig. 16(d), the spectral features due to saccharin can be identified (refer to Fig. 17). This allows a refined detection map to be generated by taking the dot-product of the spectra shown in Fig. 16(d) with each pixel in the hypercube. Finally, a threshold is set to decide which pixels actually contain the contamination to create a binary detection map (if needed). Note that the detection map is not correlated with the single frame of the reflectance hypercube [Fig. 16(a)], which only represents the sample's reflectance intensity but not its spectral shape.

In one set of government administered tests, saccharin, RDX, and PETN were applied using a dry transfer method onto a wide range of substrates such as rubber, polished aluminum, painted drywall, polyurethane, cotton cloth, wood, cardboard, plastic, canvas, leather, and packing tape. The mass loadings that were used were 10 and 50 $\mu$g. The coverage area was not well controlled because of variability in the dry-transfer method, but the contamination was typically spread over an area of 1 to 10 mm$^2$. This corresponds to localized regions with areal concentrations on the order of 100 to 1000 $\mu$g/cm$^2$. Measurements were made at close range with GSD = 80 $\mu$m, and it was found that the contaminant could be distinguished from the clean substrate for all of the substrates tested. Figure 17 shows the scaled and offset reflection spectra for 10 $\mu$g of saccharin on a wide variety of substrates. In all cases, the spectral features due to saccharin are clearly observed regardless of the substrate. The fact that the spectra are so similar is indicative of its high local concentrations.

Figure 18 shows an example of a caffeine-contaminated fingerprint on a cell phone case that is measured at close range. The fingerprint was made using a synthetic thumb from NRL in which the skin oils are simulated using Crambe oil. The synthetic thumb was contaminated by bringing it into contact with caffeine powder. Under normal lighting conditions, the fingerprint was not visible to the naked eye. The visible image that is shown was taken under conditions that particularly highlighted the fingerprint. One is able to see the fingerprint and resolve the fingerprint ridges from the mean intensity in the reflection hypercube. After performing spectral analysis, the signature due to caffeine is clearly observed. Note that caffeine is localized toward the lower, central portion of the fingerprint and that the edges of the fingerprint were not contaminated.

The next examples demonstrate detection of PETN that is dry transferred onto a computer keyboard key. Figure 19 shows a visible image of 0.2 $\mu$g of PETN that is transferred to the keyboard in a highly localized area of <1 mm$^2$. Measurements were made at close range with GSD = 80 $\mu$m. The detection map shows that PETN was detected in 33 pixels. Therefore, assuming that the total mass of the PETN that was deposited is 0.2 $\mu$g, then the system is able to detect 6 ng on a per-pixel basis. In fact, it is likely that the total mass of the PETN is even less than this because the transfer efficiency of the deposition method can be less than unity. Figure 20 shows the case where 50 $\mu$g of PETN was dry transferred to a keyboard. The

(a) Visible image

(b) Hypercube (mean reflectance)
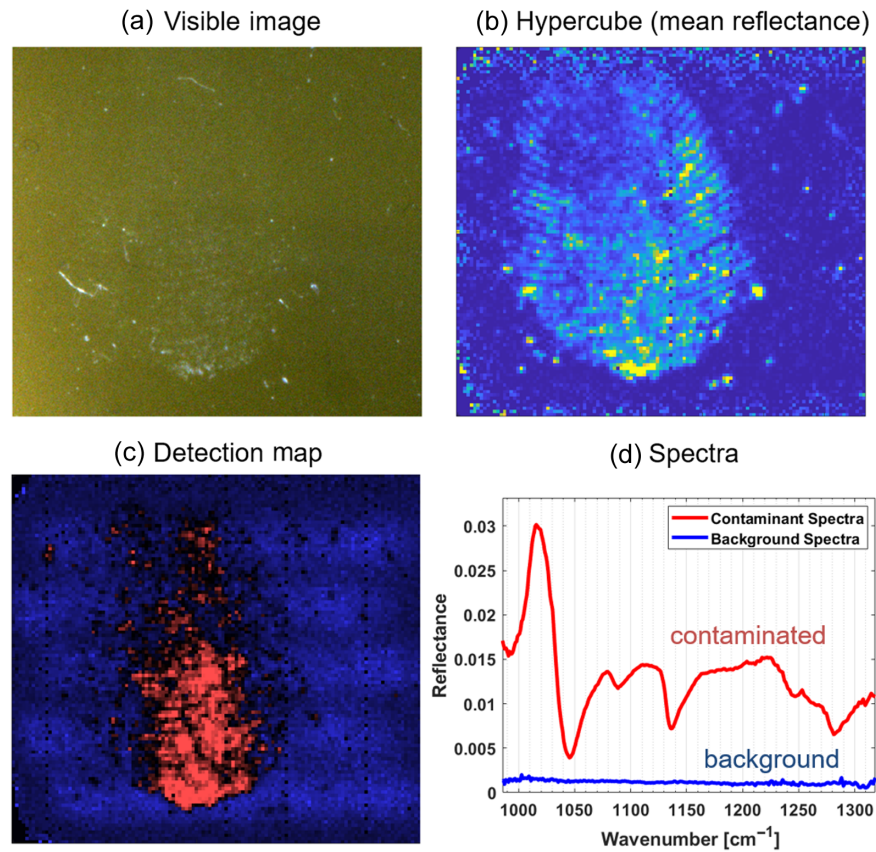
(c) Detection map

(d) Spectra

**Fig. 18** Example of a caffeine-contaminated fingerprint on a cell phone case which shows the (a) visible image of the contamination, (b) the mean reflectance from the LWIR hypercube, (c) the resulting detection map, and (d) a comparison of the spectra in the clean and contaminated regions.
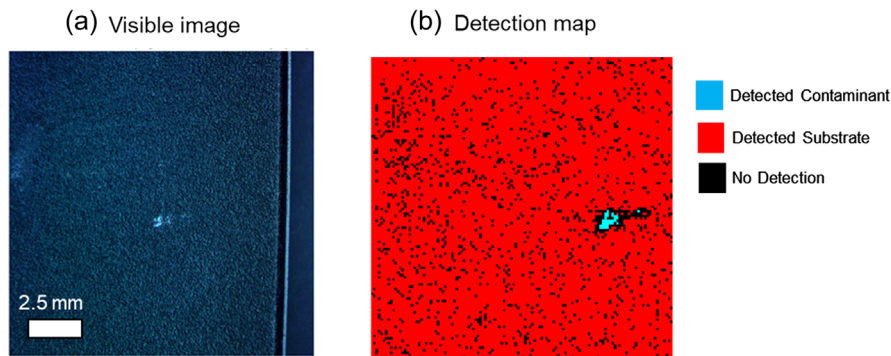
(a) Visible image

(b) Detection map

**Fig. 19** Example of detecting 0.2 $\mu$g of PETN that was dry transferred onto a computer keyboard in which (a) shows a visible photomicrograph of the contamination, and (b) the detection map.

reflectance signature for the PETN is similar to that of bulk powder reflectance given its high local concentration. The sample was then wiped four times using an isopropanol-soaked cloth in an effort to remove the PETN. Even after wiping, a residue of PETN remains behind because it is difficult to remove given that the keyboard surface is slightly rough. As a result, it is still possible to detect and identify the presence of the PETN. Interestingly, the shape of the reflection spectrum changes from that of a bulk powder to that of a thin film on a dielectric substrate. This would be expected when the PETN is dissolved in the isopropanol and redeposited onto the surface. In both cases, the chemical can be identified as PETN based on the location of the spectral features.
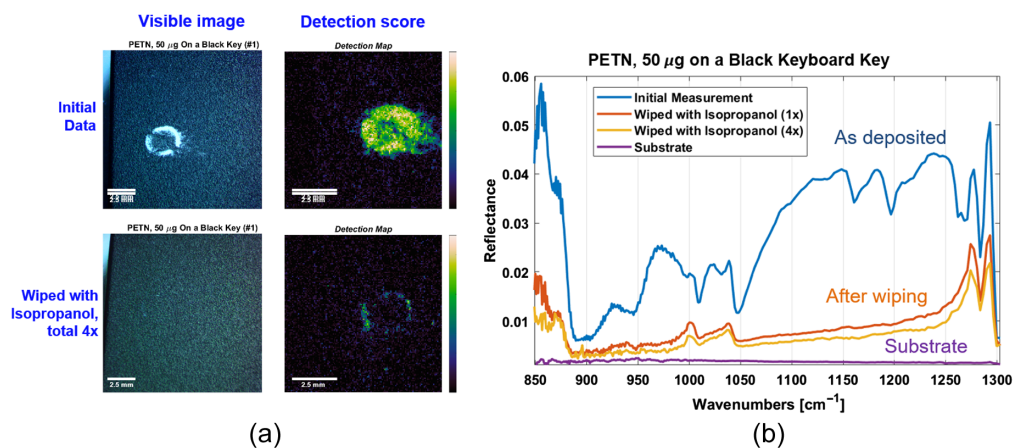
**Fig. 20** Example of detecting PETN on a computer keyboard both before and after wiping with a solvent. (a) the images on the left show visible photomicrographs and detection maps for the cases where the PETN was as deposited and after wiping with an isopropanol-soaked cloth. (b) shows the measured reflection spectra for the underlying substrate and for the PETN as deposited and after being wiped away.
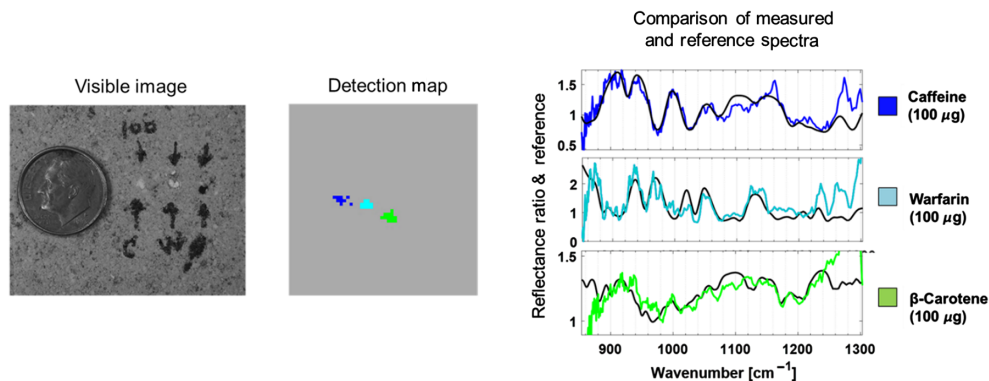


**Fig. 21** Example of detecting and identifying three different chemicals on concrete at 5-m standoff.

The final example, shown in Fig. 21, is of the dry transfer of 100 $\mu$g of three different chemicals (caffeine, warfarin, and $\beta$-carotene) onto concrete. This sample was measured at a standoff distance of 5 m with GSD = 1 mm. The reflection spectrum for each chemical is normalized with respect to the reflection spectrum of the concrete substrate. After this normalization step, it is found that the spectra correlate with the bulk powder reflectance. As a result, it was possible to detect, identify, and map each of these chemicals.

## 4 Summary

In summary, laser-based LWIR hyperspectral imaging is shown to be a powerful method for the standoff detection, identification, and mapping of trace chemicals on surfaces. It is our opinion that LWIR reflectance spectroscopy is uniquely suited to combining high-sensitivity chemical detection with the ability to rapidly scan surfaces with high ACR while remaining eye safe. A greater understanding of the spectral signatures as well as development of the associated component technologies has been greatly advanced under the IARPA SILMARILS program. The results to date indicate that the detection performance depends on the combination of chemical, chemical presentation, and substrate. Nevertheless, for most chemical and substrate combinations, the detection limit tends to fall in the range of 1 to 100 $\mu$g/cm$^2$. At close range where measurements can be made with high spatial resolution, it is possible to measure nanogram-class amounts of contamination. There are two situations that are particularly favorable for high-sensitivity detection: (i) particulates on an otherwise smooth surface and (ii) thin film on a

dielectric substrate. For both of these cases, limits of detection on the order of 0.1 $\mu$g/cm$^2$ should be possible. By contrast, the case of detecting contamination on polymeric fabrics can be challenging due to both the scattering nature of the substrate and its variable spectral properties.

## Acknowledgments

## References

1. K. DeWitt, "Advances in active infrared spectroscopy for trace chemical detection," *Proc. SPIE* **10986**, 109860J (2019).
2. P. M. Pellegrino, E. L. Holthoff, and M. E. Farrell, *Laser-Based Optical Detection of Explosives*, CRC Press, Boca Raton (2015).
3. A. Venter, M. Nefliu, and R. G. Cooks, "Ambient desorption ionization mass spectrometry," *Trends Anal. Chem.* **27**, 284–290 (2008).
4. Y. Seto et al., "Sensing technology for chemical-warfare agents and evaluation using authentic agents," *Sens. Actuators B* **108**, 193–197 (2005).
5. A. W. Fountain, III et al., "Long range standoff detection of chemical and explosive hazards on surfaces," *Proc. SPIE* **7484**, 748403 (2009).
6. J. Gottfried et al., "Laser-induced breakdown spectroscopy for detection of explosives residues: a review of recent advances, challenges, and future prospects," *Anal. Bioanal. Chem.* **395**, 283–300 (2009).
7. A. Ford et al., "Extension of a standoff explosives detection systems to CBRN threats," *Proc. SPIE* **7665**, 76650Y (2010).
8. M. Wu et al., "Stand-off detection of chemicals by UV Raman spectroscopy," *Appl. Spectrosc.* **54**, 800–806 (2000).
9. P. Ponsardin et al., "Expanding applications for surface-contaminant sensing using the laser interrogation of surfaces agents (LISA) technique," *Proc. SPIE* **5268**, 321–327 (2004).
10. S. D. Christesen et al., "UV Raman spectra and cross sections of chemical agents," *Proc. SPIE* **6218**, 621809 (2006).
11. S. Sharpe et al., "Infrared spectral signatures: creation of reference data for vapors and liquids," *Int. J. High-Speed Electron. Syst.* **18**, 231–250 (2008).
12. B. M. DeVetter et al., "Reflectance from solids and solid particles: the need for the optical constants $n$ and $k$ and far-IR measurement challenges," *Proc. SPIE* **10750**, 1075008 (2018).
13. J. M. Theriault et al., "Passive standoff detection of liquid surface contaminants: recent results with CATSI," *Proc. SPIE* **5268**, 310–320 (2004).
14. V. Farley et al., "Chemical agent detection and identification with a hyperspectral imaging infrared sensor," *Proc. SPIE* **6739**, 673918 (2007).
15. C. M. Gittins and W. J. Marinelli, "AIRIS multispectral imaging chemical sensor," *Proc. SPIE* **3383**, 65–74 (1998).

16. A. K Goyal and T. R. Myers, "Active mid-infrared reflectometry and hyperspectral imaging," in *Laser-Based Optical Detection of Explosives*, P. M. Pellegrino, E. L. Holthoff, and M. E. Farrell, Eds., pp. 167–211, CRC Press, Boca Raton (2015).
17. M. C. Phillips and B. E. Bernacki, "Infrared spectroscopy of explosives residues: measurement techniques and spectral analysis," in *Laser-Based Optical Detection of Explosives*, P. M. Pellegrino, E. L. Holthoff, and M. E. Farrell, Eds., pp. 213–255, CRC Press, Boca Raton (2015).
18. F. Fuchs et al., "Infrared hyperspectral standoff detection of explosives," *Proc. SPIE* **8710**, 87100I (2013).
19. A. K. Goyal et al., "Active hyperspectral imaging using quantum cascade laser (QCL) array and a digital-pixel focal plane array (DFPA) camera," *Opt. Express* **22**, 14392 (2014).
20. A. K. Goyal et al., "Active infrared multispectral imaging of chemicals on surfaces," *Proc. SPIE* **8018**, 80180N (2011).
21. D. B. Kelley et al., "High-speed mid-infrared hyperspectral imaging using quantum cascade lasers," *Proc. SPIE* **10183**, 1018304 (2017).
22. D. B. Kelley et al., "High-speed and large-area scanning of surfaces for trace chemicals using wavelength-tunable quantum cascade lasers," *Proc. SPIE* **10629**, 1062909 (2018).
23. D. Wood et al., "Mid-infrared reflection signatures for trace chemicals on surfaces," *Proc. SPIE* **10629**, 1062915 (2018).
24. T. Meyers et al., "Mid-infrared hyperspectral simulator for laser-based detection of trace chemicals on surfaces," *Proc. SPIE* **10198**, 101980C (2018).
25. G. Raz et al., "Optimal sensor control for fast target detection in hyperspectral imagery," *Proc. SPIE* **10644**, 1064407 (2018).
26. M. C. Phillips and N. Ho, "Infrared hyperspectral imaging using a broadly tunable external cavity quantum cascade laser and microbolometer focal plane array," *Opt. Express* **16**, 1836 (2008).
27. M. F. Witinski et al., "Standoff hyperspectral imaging of CWAs and explosives using eye-safe quantum cascade laser arrays," *Proc. SPIE* **11010**, 1101003 (2019).
28. C. J. Breshike et al., "Infrared backscatter imaging spectroscopy for standoff detection of trace explosives," *Proc. SPIE* **11010**, 1101004 (2019).
29. C. R. Howle et al., "Active hyperspectral imaging system for the detection of liquids," *Proc. SPIE* **6954**, 69540L (2008).
30. C. A. Kendziora et al., "Photothermal methods for laser-based detection of explosives," in *Laser-Based Optical Detection of Explosives*, M. Pellegrino, E. L. Holthoff, and M. E. Farrell, Eds., pp. 257–287, CRC Press, Boca Raton (2015).
31. C. A. Kendziora et al., "Infrared photothermal imaging of trace explosives on relevant substrates," *Proc. SPIE* **8709**, 87090O (2013).
32. A. Mukherjee, S. Von der Porten, and C. K. N. Patel, "Standoff detection of explosive substances at distances of up to 150 m," *Appl. Opt.* **49**, 2072 (2010).
33. L. A. Skvortsov and E. M. Maksimov, "Application of laser photothermal spectroscopy for standoff detection of trace explosive residues on surfaces," *Quantum Electron.* **40**, 565 (2010).
34. T. Myers et al., "Mid-infrared hyperspectral simulator for laser-based detection of trace chemicals on surfaces," *Proc. SPIE* **10198**, 101980C (2017).
35. M. C. Phillips et al., "Challenges of infrared reflective spectroscopy of solid-phase explosives and chemicals on surfaces," *Proc. SPIE* **8358**, 83580T (2012).
36. R. Furstenberg et al., "Synthetic models for infrared reflectance signatures of micro-particle traces on surfaces," *Proc. SPIE* **11010**, 110100K (2019).
37. H. Macleod, *Thin-Film Optical Filters*, CRC Press, Boca Raton (2010).
38. L. C. Pacheco-Londono et al., "Angular dependence of source-target-detector in active mode standoff infrared detection," *Proc. SPIE* **8711**, 871108 (2013).
39. C. A. Ortega-Zuniga et al., "Dependence of detection limits on angular alignment, substrate type and surface concentration in active mode standoff IR," *Proc. SPIE* **8734**, 87340R (2013).

Biographies of the authors are not available.